Energy Conversion and Management 256 (2022) 115404

Contents lists available at ScienceDirect

Energy Conversion and Management

journal homepage: www.elsevier.com/locate/enconman

A proof-of-concept study of a novel ventilation heat recovery vapour injection air source heat pump

Yi Fan [a,b], Jing Li [b,*,1], Xudong Zhao [b,*,1], Steve Myers [b], Yuanda Cheng [c], Min Yu [b], Yousef Golizadeh Akhlaghi [d], Xiaoli Ma [b], Sen Yu [a]

[a] *College of Energy and Mechanical Engineering, Shanghai University of Electric Power, 1851 Hucheng Road, Shanghai, China*
[b] *Research Centre for Sustainable Energy Technologies, University of Hull, Hull HU6 7RX, UK*
[c] *College of Environmental Science and Engineering, Taiyuan University of Technology, 030024, China*
[d] *Renewable Energy, Building Energy, Data Science, Newcastle University, Newcastle NE1 7RU, UK*

ARTICLE INFO

Keywords:
Vapour injection heat pump
Air source heat pump
Ventilation heat recovery
Defrost
Coefficient of performance

ABSTRACT

Conventional air source heat pumps suffer from frosting in winter and consume a large amount of electricity for defrosting. Meanwhile, ventilation heat recovery is an important approach to energy saving in buildings. This paper conducts a proof-of-concept study of a novel ventilation heat recovery vapour injection air source heat pump. A prototype is built and tested. It has a unique defrosting process driven by the warm exhaust air from buildings. In the normal operation, the exhaust air is first cooled down by a medium-pressure evaporator. It is then mixed with the ambient air to heat the low-pressure evaporator. Both theoretical simulation and experimental validation are carried out. The results show that the proposed heat pump can significantly decrease the thermodynamic irreversibility and electricity consumption, thus leading to a higher efficiency. For the novel heat pump, the coefficient of performance increased from 3.8 to 4.5 when the ambient temperature varied from −5°C to 10 °C. Furthermore, the defrosting process using exhaust air is fast and efficient. The defrosting duration (within 4 mins) is less than 30% of the frosting period at 0 °C, with little power consumption. Consequently, the prototype has demonstrated an enhanced performance with high flexibility and feasibility. It tackles the challenges of conventional air source heat pumps and is promising in the cold climate area application.

1. Introduction

In recent years, environmental pollution problems caused by power generation systems using fossil fuels have been attracting more attention [1]. With the increasing global warming concerns and increasing contribution of building energy consumption, building energy efficiency has become the focus of attention worldwide [2]. Among all building services, Heating, Ventilation, and Air Conditioning (HVAC) systems are responsible for the majority of building energy use [3]. In HVAC, ventilation is a key element for providing suitable indoor air quality, and it uses significant amounts of energy within buildings [4]. Energy consumed by room ventilation accounts for 30–60% of the total energy consumption of buildings [5]. Thus, improving ventilation systems plays an important role in improving the energy efficiency of buildings and in providing a better indoor condition for the occupants [6]. In recent years, many energy efficiency optimisation strategies and technologies have been proposed and applied to mitigate energy waste from the building ventilation systems [7].

The energy efficiency of a ventilation system is interrelated with many factors such as indoor and outdoor conditions, building characteristics, building applications as well as occupants' behaviour [8]. Despite the investigations carried out on these factors for saving building energy consumption in recent years, adding heat recovery devices to a building ventilation system for recovering energy from the exhaust air is considered an important way to improve energy efficiency [9]. Heat recovery devices can efficiently decrease the energy consumption of the buildings by more than 20% [10], and recover about 60% to 95% of the heat in the exhaust air without limiting or affecting the function of the buildings [11]. From the perspective of the system operation, the heat recovery systems include passive and active heat recovery systems [12]. It is shown in the literature that the active heat recovery systems, like a heat recovery heat pump (HRHP), are more efficient to reduce the energy consumption, recover exhaust heat, remove pollutants, and provide

---

[*] Corresponding authors.
E-mail addresses: Jing.li@hull.ac.uk (J. Li), Xudong.Zhao@hull.ac.uk (X. Zhao).

[1] The two authors have the same contribution to this study.

https://doi.org/10.1016/j.enconman.2022.115404
Received 11 November 2021; Received in revised form 16 February 2022; Accepted 17 February 2022

Nomenclature

ASHP	Air source heat pump;
COP	Coefficient of performance
Cp	Specific heat, J/(kg·°C);
E_d	Exergy destruction during the throttling process, J;
EEV	Electronic expansion valve;
ELA	Evaporation line aperture;
h	Enthalpy of the refrigerant, J/kg;
HP	Horse power;
HRHP	Heat recovery heat pump;
HRVI-ASHP	Heat recovery vapour injection air source heat pump;
HVAC	Heating, Ventilation, and Air Conditioning;
IHX	Inner heat exchanger;
m_w	Mass flow rate of the water in water tank circulation, kg/s;
m_{ref}	Mass flow rate of the refrigerant in the heat pump, kg/s;
P	Pressure, MPa;
$Q_{hp.c}$	Collected heat of the water tank, kW;
$Q_{hp.g}$	Heat generated by the heat pump, kW;
R	Compression ratio;
s	Entropy of refrigerant, J/°C•kg;
$T_{con.out}$	Condenser outlet temperature in water tank circulation, °C;
$T_{con.in}$	Condenser inlet temperature in water tank circulation, °C;
T_{am}	Ambient temperature, °C;
VI	Vapour injection;
VIHP	Vapour injection heat pump;
VILA	Vapour injection line aperture;
W_{hp}	Power dissipation of the heat pump, kW;

Subscripts

dp	Discharge pressure of the compressor
epl	Evaporation line
fcr	Final compression ratio
hp	Heat pump
icr	Intermediate compression ratio
o	Outlet
u	Inlet
vil	Vapour injection line

adequate ventilation to buildings [13]. At present, many energy-efficient buildings adopt heat pump systems for heat recovery, such as apartment buildings [14], nearly zero-energy buildings [15], multi-family houses [16], school buildings [17], and are also used in nearly all newly built family houses in Europe for exhaust air heat recovery [18].

As a hot spot of current research topics, HRHPs have been investigated by many researchers. Wang et al. conducted an exergoeconomic performance analysis of an industrial HRHP system using Aspen Plus. The result showed that HRHP based on the exergoeconomic device choosing criterion can achieve better thermodynamic (exergy-based) and economic performance [19]. Garayo et al. combined the heat pump with a heat recovery heat pump for a passive house dwelling which significantly improved the COP (2–3 times for partial load operation and 12.5 % for maximum load) [20]. Tan et al. compared the performance of different low-temperature HRHPs. The results showed that while the heat ratio was higher than about 0.5, the mechanical heat pump had the best energy performance. When the heat ratio was lower than about 0.5, the absorption heat transformer was the best [21].

Besides, in order to further improve the performance of HRHP systems, some researchers have carried out optimisation studies. Wang et al. proposed a study on a triplex loop HRHP for exhaust air. The experiment was conducted in winter conditions (−20 °C ambient temperature) and the COP of the system can reach 9.33 [22]. Stefan et al. proposed a two-stage air source heat pump that provided the capability to increase the performance of the exhaust air heat pump [23]. The proposed two-stage or three-stage compression heat pump system can increase the performance of the heat recovery heat pump. However, the cost and complexity of the system were greatly increased by adding one or two compressors. To improve the performance with one compressor, Saini et al. investigated an HRHP assisted by unglazed transpired solar collectors to preheat the ambient air, discovering the new system had a small but positive impact on the overall system performance [24]. Jia et al. proposed a parallel-loop heat pump with a dual-cylinder rotary compressor, resulting in a greatly improved performance level of the heat pump system for ventilation heat recovery by using the novel compressor with independent suction and discharge ports [25]. Although the exhaust air heat pumps have been extensively developed and examined, the HRHPs also present some problems. Essentially, as the limited flow rate of the exhaust air from a building, the heating capacity of an HRHP is low [26]. Accordingly, the HRHP system often requires an auxiliary plant, as they are only able to cover a relevant fraction of the thermal/cooling energy requirements for air-conditioning [27].

Compared with the HRHP, ASHP has been more widely applied in supplying building heating, cooling, and hot water due to its effectiveness in utilising the unlimited amount of ambient air as the energy source [28]. Thus, it can potentially provide enough heating and cooling energy without an auxiliary heating device, which is an advantage over the HRHPs. However, when it comes to operation in cold regions, the ASHPs perform poorly due to the low coefficient of performance (COP) and large power consumption for defrosting [29].

In summary, the ASHP and the HRHP have been studied extensively. The two types of heat pumps have their own pros and cons. In order to overcome the limitation of heating capacity of conventional exhaust air heat pumps and fulfill the energy demand of buildings, a heat recovery vapour injection air source heat pump (HRVI-ASHP) is proposed in this paper. In the authors' previous study the concept of this novel heat pump has been briefly introduced and the initial simulation has shown an enhanced performance compared with the conventional vapour injection heat pump [30]. However, the real-time performance of the HRVI-ASHP has yet to be demonstrated. To this end, a proof-of-concept study of the proposed heat pump is conducted in this paper. A prototype is developed and valuable test data on the practical use of this novel heat pump are presented.

2. Description of the novel heat recovery vapour injection air source heat pump

The composition and working principle of the HRVI-ASHP are shown in Fig. 1. The system is mainly composed of six individual components: a vapour injected compressor, an internal heat exchanger (IHX), a coil heat exchanger (condenser), two electronic expansion valves (EEVs), two evaporators and a refrigerant storage tank. The main components and details for the HRVI-ASHP are shown in Table 1.

In order to fully utilise the exhaust heat from buildings, the HRVI-ASHP is innovatively fitted with an evaporator (Evaporator 1) after the EEV1 along the vapour injection line in order to directly extract a part of the heat from the exhaust air. The refrigerant in the vapour injection line will also acquire a part of the heat in the internal heat exchanger (IHX), thus leading to sub-cooling in the evaporation line. When it comes to the air path, after going through Evaporator 1, the exhaust air still contains useable heat and is mixed with the ambient air to increase the heating capacity. The mixed air will go through

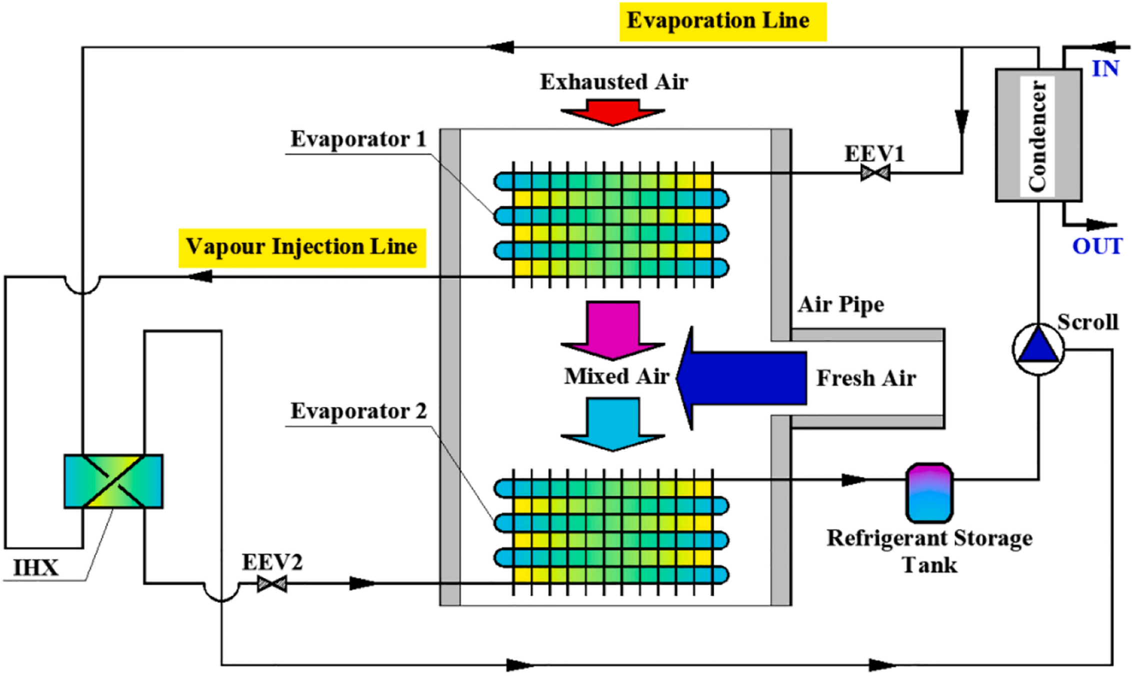

Fig. 1. Composition and working process of the HRVI-ASHP device.

Table 1
The main components and details of the novel HRVI-ASHP.

Component	Number	Brand	Detail
Compressor	1	Emerson, USA	Vapour injection compressor (ZW059HSP) Refrigerant: R410A; Power 3HP; Power supply: 220 V(AC).
Internal heat exchanger	1	Debao, China	Brazed Plate Heat Exchanger (HL20-30D) Heat transfer capacity: 73 kW to 97 kW; Dimensions: 10 cm*30 cm; Plate number: 30.
Condenser	1	Ancool, China	Shell-and-tube heat exchanger (155CS070) Media: refrigerant and water.
Expansion valve	2	Sanhua, China	Electronic expansion valve (DPF(Q) 2.4C-11RK) Media temperature: −30 °C to 70 °C; Working temperature: −30 °C to 60 °C.
Evaporator 1	1	Qingli, China	Air heating evaporator Location: vapour injection line; Dimensions: 73 cm*66 cm; Tube row number: 3.
Evaporator 2	1	Qingli, China	L-type air heating evaporator Location: evaporation line; Dimensions: 70 cm*33 cm*1200 cm; Tube row number: 2.
Refrigerant storage tank	1	Hong Yuan, China	Liquid-vapour separator (KFR120WLG-OLA) Volume: 2.8L.
Axial flow fan	2	Huayang, China	Nominal voltage: 220 V (YDK-90–6) Rated power: 90 W Rated revolving speed: 750r/min

Evaporator 2 in the evaporation line. This two-stage evaporation can greatly increase the exhausted energy utilisation, and thus increase the performance of the HRVI-ASHP.

The rendered view of the HRVI-ASHP from the front and the back is shown in Fig. 2. At the front, there are two draught fans for heat transfer in Evaporator 2. Under the devices and controller cover, there is the heat pump controller which controls the operation of the HRVI-ASHP components. In addition, EEVs, IHX, condenser, compressor, and refrigerant storage tank are all installed in this chamber. On the side of the HRVI-ASHP, there are two pressure gauges that show the pressure of the compressor outlet (high pressure) and the compressor inlet on the evaporation line (low pressure), which can be used to calculate the final compression ratio of the heat pump. Similarly, the back view of the HRVI-ASHP is shown in Fig. 2(b). Evaporator 1 is connected with the vapour injection line and is heated by the exhaust air duct. A meshed screen is installed in the mixing chamber, which helps the fresh air and the exhaust air to mix evenly.

3. Comparison between the conventional and novel vapour injection cycles

The schematic diagram of the novel HRVI-ASHP is shown in Fig. 3. Different from the conventional VIHP, the novel HRVI-ASHP adds an evaporator into the vapour injection line between EEV1 and the IHX (the red component shown in Fig. 3). In the compression process of the conventional VIHP, the superheated refrigerant vapour from the compressor (State 1) enters the coil heat exchanger (condenser), where the vapour is condensed to State 2. The liquid refrigerant leaving the condenser (State 2) is separated into two pipelines (the vapour injection line and the evaporation line). After the refrigerant has expanded through EEV1 in the vapour injection line to State 3, it flows directly to the IHX, and is heated to State 5 by the refrigerant from Point 2 in the evaporation line, and sucked into the compressor through the injection port. Because the refrigerant enthalpy at State 2 in the evaporation line is limited, the refrigerant mass flow rate in the vapour injection line is quite restricted. In the evaporation line, after the IHX, the refrigerant reaches State 6. Then, it experiences an expansion process through EEV2 to State 7′. Finally, superheated by the air in the evaporator to State 8′, the refrigerant is sucked into the compressor through the suction port.

The compression process of the HRVI-ASHP is similar to that of the conventional VIHP from State 1 to State 2. The refrigerant in the vapour injection line goes through EEV1 first to State 3 and then partially evaporates in Evaporator 1 to State 4 by extracting the heat from the exhaust air from the building. The refrigerant then flows to the IHX to absorb a part of the heat from the evaporation line to State 5 and finally

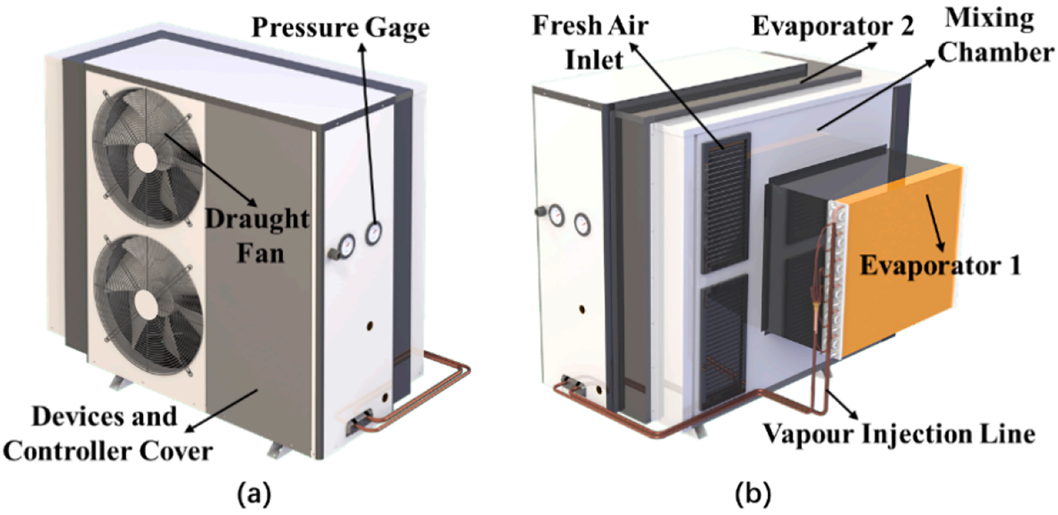

Fig. 2. (a) Front view of the HRVI-ASHP. (b) Back view of the HRVI-ASHP.

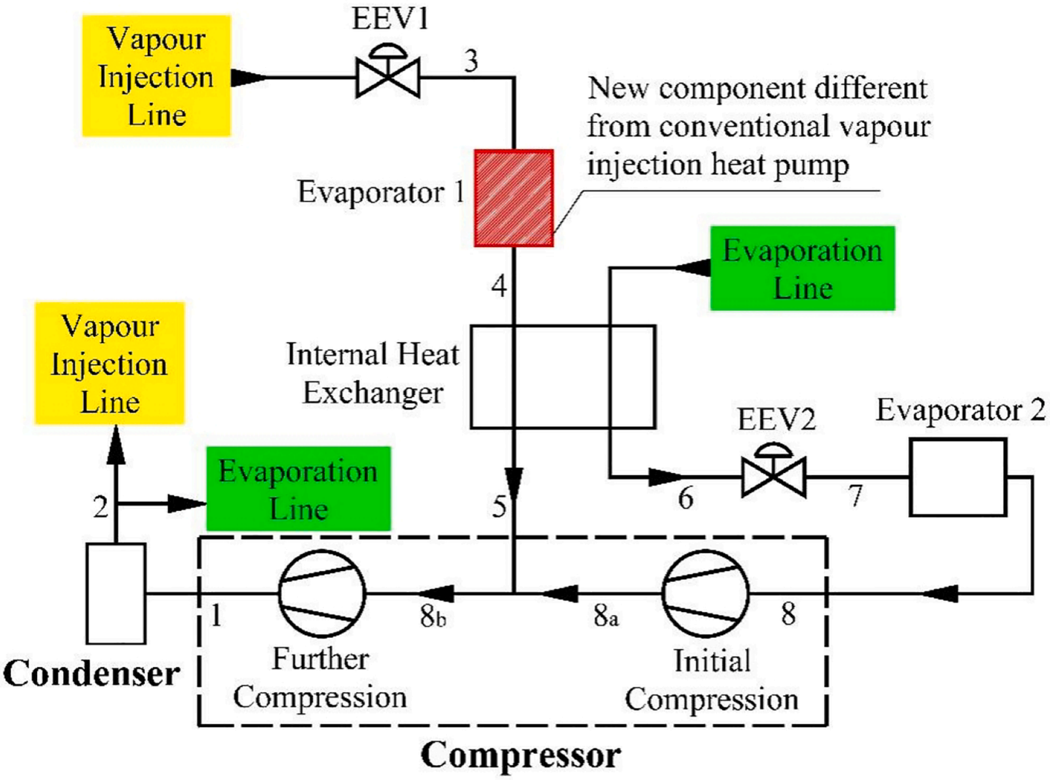

Fig. 3. Schematic of the conventional and novel vapour injected compression process.

goes into the vapour injection compressor. In addition to the vapour injection line after the condenser, a proportion of the refrigerant follows the evaporation line and releases heat in the IHX (State 6). The refrigerant goes through EEV2 to State 7. Then, the evaporation process takes place in Evaporator 2 (State 8) by absorbing the heat from the mixture of the fresh air and the exhaust air coming from Evaporator 1. Finally, after going through the refrigerant storage tank, the refrigerant vapour returns to the compressor.

In the vapour injection compressor, the vapour refrigerant from the evaporation line is first compressed, and then is mixed with the refrigerant vapour from the vapour injection line. The mixed refrigerant vapour is further compressed to the discharge pressure (State1).

P-h diagram for the conventional vapour injection (VI) cycle and the novel heat recovery vapour injection (HRVI) cycle is shown in Fig. 4. The difference between the conventional VI cycle and the HRVI cycle is in the compression line, where the conventional VI cycle's evaporating pressure (depicted as the red dashed lines) is lower than the HRVI cycle's evaporating pressure (depicted as the black solid lines). Unlike the conventional VI cycle, there is an evaporator in the vapour injection line in the novel HRVI-ASHP. The added evaporator in the vapour injection line can significantly increase the vapour injection rate and the mixed air can elevate the temperature in Evaporator 1. Hence, the equivalent pressure ratio of the compressor is decreased. The T-S diagram for the conventional VI cycle and the novel HRVI cycle is shown in Fig. 5. The

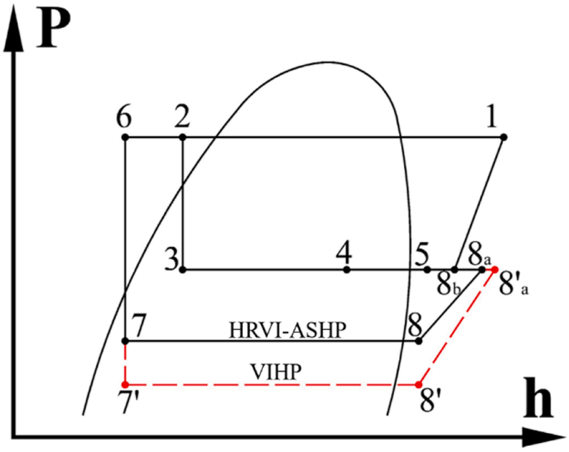

Fig. 4. P-h diagram for the conventional VIHP and the novel HRVI-ASHP.

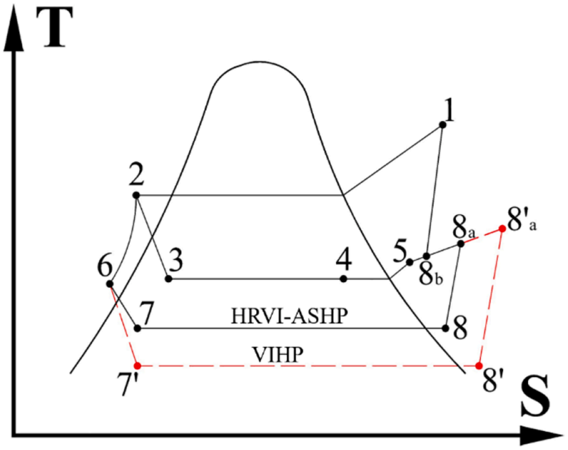

Fig. 5. T-S diagram for the conventional VIHP and the novel HRVI-ASHP.

HRVI cycle has a higher overall evaporation temperature than the VI cycle, leading to a higher COP at the given ambient air temperature and condensation temperature.

For a better comparison between the novel heat pump and conventional air source heat pump, the thermodynamic irreversibility is examined, especially for the throttle valves. The exergy destruction during the throttling process is expressed by

$$E_d = m_{ref}(s_o - s_i)T_0 \tag{1}$$

s_i and s_o are the inlet and outlet entropy; T_0 is the ambient temperature and m_{ref} is the mass flow rate of the refrigerant. For a conventional air source heat pump, there is only one throttle valve. For the novel heat pump, E_d is the sum of exergy destruction in the two throttle valves.

E_d is caused by the pressure drop of the refrigerant and is proportional to $\int_{p_o}^{p_i} vdp$,

$$E_d \propto \int_{po}^{pi} vdp \tag{2}$$

p_i and p_o are the inlet and outlet pressure of the valve. v is the specific volume, which increases with the increment in the vapour fraction.

4. Experimental setup

The experimental platform of the HRVI-ASHP was set up in a specialised heat pump laboratory as shown in Fig. 6. The laboratory can control the indoor temperature and humidity at a relatively stable level.

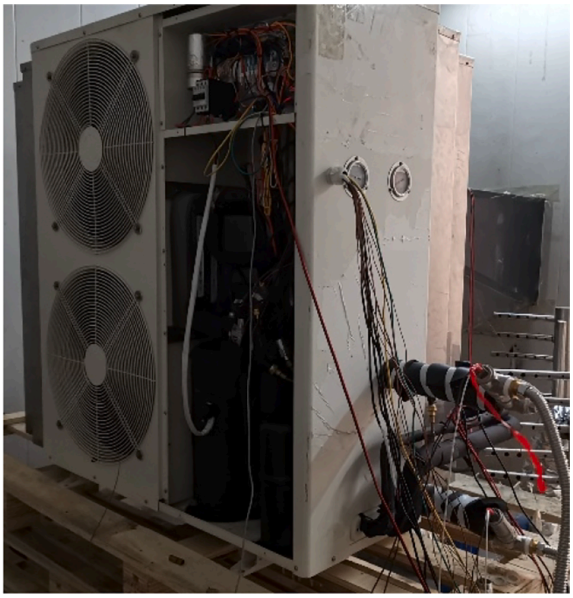

Fig. 6. Experimental platform of the HRVI-ASHP.

4.1. Experimental procedure

The experiment was designed to simulate the winter conditions with low winter ambient temperature (around −15 °C to 10 °C). During this experiment, the relative humidity of the laboratory environment was set at 60%, and according to the accuracy of the laboratory control system, the relative humidity of the laboratory environment could change between 57% and 63%. The experiment was running from October to December 2019 in Dongguan City, Guangdong Province, China (23.02°N, 113.75°E). During the experiment period, the local ambient temperature was relatively stable in the daytime (around 24 °C), which was in accordance with the building exhaust air temperature requirements. The range of the ambient environment relative humidity was wider than that of the laboratory, which varied between 65% and 80%. Hence, instead of using the laboratory to provide exhaust air, the laboratory outdoor air was treated as the exhaust air for this experiment. To achieve this aim, the exhaust air inlet of the air source heat pump was connected to the window of the laboratory by using an exhaust air duct, as shown in Fig. 7.

The laboratory can maintain the indoor temperature and humidity at a certain level (relative humidity: ±3%, laboratory temperature: ±1°C) using the laboratory controlling devices shown in Fig. 8(a), which can conveniently support the steady-state experiment conditions. To control the airflow rate of the exhaust air at the inlet of the air source heat pump, an air volume damper was installed on the inlet of the air duct as in Fig. 8 (b). In order to avoid the interference between the laboratory's inside

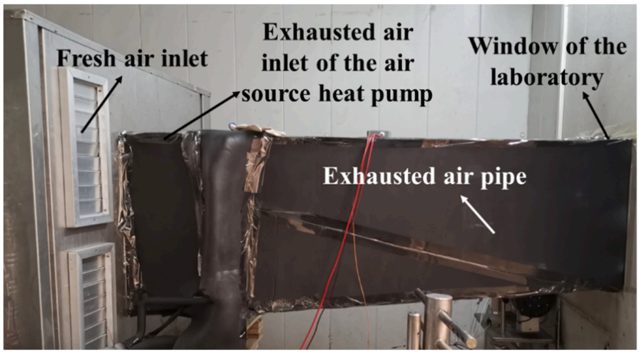

Fig. 7. Air inlets arrangement of the HRVI-ASHP.

(a) (b)

Fig. 8. (a) Laboratory environment control system. (b) Air volume damper.

and outside environments, the air duct was insulated thoroughly.

The schematic layout of the HRVI-ASHP experimental set-up and corresponding experimental instruments are shown in Fig. 9. There were two circuits between the experimental devices, i.e., HRVI-ASHP circuit and the water tank circuit. These two circuits were connected to each other in the condenser of the heat pump to complete the heat transfer cycle. For the HRVI-ASHP circuit, there were seven main components: 1. a vapour injection compressor; 2. a condenser; 3. the first EEV in the vapour injection line; 4. an evaporator in the vapour injection line; 5. an inner heat exchanger; 6. the second EEV in the evaporation line; 7. an evaporator in the evaporation line. A temperature sensor and a pressure gauge were installed between every two components along the circuit. In addition, an electrical parameter detector was connected to the compressor which can detect and collect the power of the compressor in real-time, and the collected data were transferred to a data logger, then saved into a computer.

The water tank circulation line connected the condenser of the heat pump with a 4 tons water tank, which can release the heat from the HRVI-ASHP to the water tank for heat storage purposes. Two temperature sensors and a mass flow rate meter were installed in the circulation line to calculate the heat from the heat pump. Four temperature sensors were situated in the water tank to monitor the temperature variation of the tank water. To maintain the water tank temperature at a certain level, water from the city supply network was injected into the water tank continuously with a relatively constant temperature. A water tank drain outlet was used to maintain the volume of the water tank and avoid the overflow. The specifications of experimental devices are shown in Table 2.

In addition to the data collected from the two circuits, the environmental parameters of the experiment were also recorded. In order to monitor these parameters, two temperature sensors are placed in the heat pump laboratory to measure the room temperature and the exhaust air duct temperature. A flow velocity sensor was also installed in the exhaust air duct to calculate the air volume flow rate (where the sectional area of the air duct was 0.34 m^2). Furthermore, an electrical parameter detector was connected to the fan to monitor the power consumption.

All the outputs of the sensors and instruments were transmitted into a Data Logger and then stored onto the computer, as shown in Fig. 10.

The performance of the HRVI-ASHP was tested and evaluated based on several operating parameters by varying the temperature of the laboratory (fresh air), the volume flow rate of the air from the outside of the laboratory (exhaust air), the refrigerant charging capacity, and the opening degree of the two EEVs.

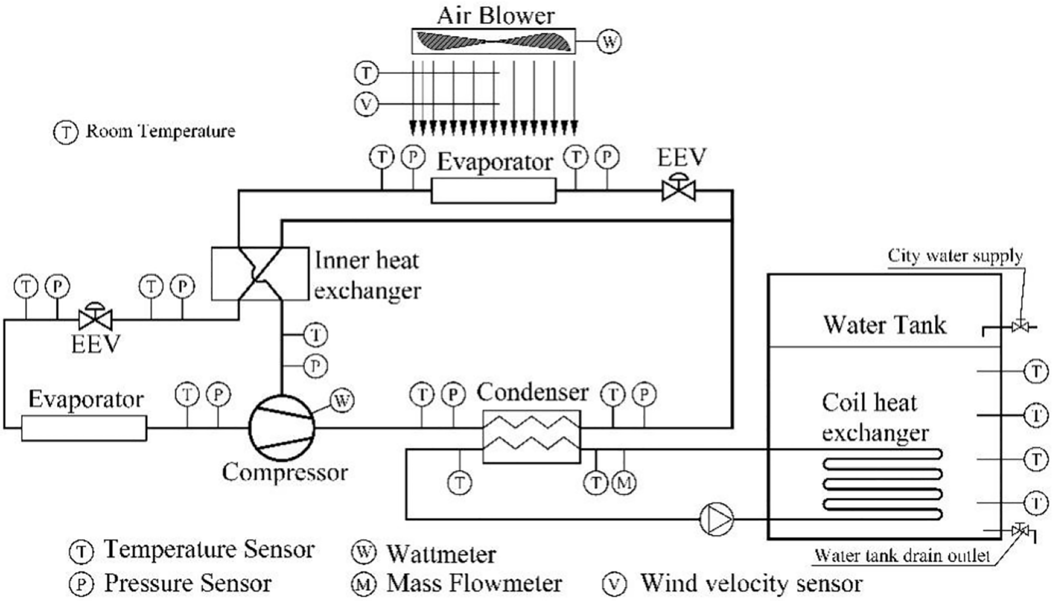

Fig. 9. Schematic of the HRVI-ASHP experimental system and experimental instruments.

Table 2
List of experimental testing and monitoring devices.

Devices	Specifications	Range	Accuracy Rate	Uncertainty	Qty.	Brand	Location
Water mass flowmeter	DN25	0–6.4 m^3/h	0.2%	±0.013 m^3/h	1	DOYI, China	Water tank loop;
Anemometer	JY-GD650	0–10 m/s	0.2%	±0.02 m/s	1	Zhongyi, China	Exhaust air duct;
Platinum resistance thermometer	PT1000	−200–350 °C	0.2%	±0.7 °C	6	Zhongjia, China	Water tank, water tank loop;
Pressure sensor	551.32	0–25 bar	0.3%	±0.075 bar	8	HUBA, Swiss	Heat pump cycle loop;
Thermocouple	TT-T-36-SLE	−200–260 °C	0.4%	±1.04 °C	10	OMEGA, USA	Heat pump cycle loop; laboratory, exhaust air duct;
Electric parameter meter	PM9802	2–600 V; 5 mA-40A	0.4%	±2.4 V ±0.16A	2	Napui, China	Air blower, compressor;
Wattmeter	PM9833A	0–5 kW	0.2%	0.01 kW	1	Napu, China	Data collecting room;
Heat pump laboratory control devices	Control box	/	/		1	Phnix, China	Data collecting room;
Data logger and computing unit	34970A	/	/		1	Agilent, USA	Data collecting room.

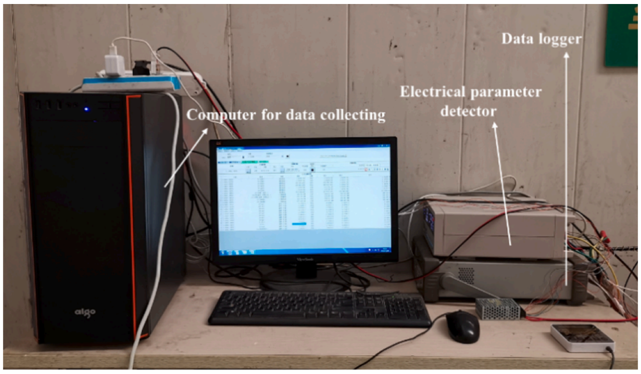

Fig. 10. Data collecting devices for the heat pump experiment.

4.2. *Performance indicators*

Instantaneous heating capacity (Q_{hp}) and *COP* [31] of the HRVI-ASHP are calculated from the following equations.

$$Q_{hp.c} = m_w Cp(T_{con.out} - T_{con.in}) \tag{3}$$

$$COP = \frac{Q_{hp.c}}{W_{hp}} \tag{4}$$

In the condenser, the relationship between the collected heat from the water tank ($Q_{hp.c}$) and the heat generated by the heat pump ($Q_{hp.g}$) are equal:

$$Q_{hp.c} = Q_{hp.g} \tag{5}$$

The generated heat ($Q_{hp.g}$) can then be expressed as [32]:

$$Q_{hp.g} = m_{ref}(h_1 - h_2) \tag{6}$$

where m_{ref} is the mass flow rate of the refrigerant in the heat pump, kg/s; h_1 and h_2 are the enthalpy of the refrigerant at the condenser inlet and the condenser outlet respectively, J/kg.

The relationship between the generated heat ($Q_{hp.g}$), the extracted heat in the vapour injection line ($Q_{hp.vil}$), the extracted heat in the evaporation line ($Q_{hp.epl}$), and the power of the heat pump (W_{hp}) can be expressed as:

$$Q_{hp.g} = Q_{hp.vil} + Q_{hp.epl} + W_{hp} \tag{7}$$

The compression ratio between the suction pressure in the evaporation line (P_{epl}) and the discharge pressure of the compressor (P_{dp}) is called the final compression ratio (R_{fcr}) [33], which can be expressed as:

$$R_{fcr} = \frac{P_{epl}}{P_{dp}} \tag{8}$$

The compression ratio between the intermediate pressure in the vapour injection line (P_{vil}) and the discharge pressure of the compressor (P_{dp}) is called the intermediate compression ratio (R_{icr}), which can be expressed as:

$$R_{icr} = \frac{P_{vil}}{P_{dp}} \tag{9}$$

4.3. *Experimental instrumentations and error analyses*

During the experiment, temperature, pressure, mass flow rate, and electric power consumption were measured, as displayed in Fig. 9. In addition, an automatic heat pump laboratory control station was used to control the environment of the lab and a data logger was used to collect the data. The specifications and accuracies for all the measuring instruments are shown in Table 2.

The directly measured parameters are m_w, W_{hp}, $T_{con.out}$ and $T_{con.in}$. The enthalpy value of the refrigerant was obtained by software REFPROP [34]. As previously mentioned, Q_{hp}, *COP* and m_{ref} are the major factors used to evaluate the system performance. The uncertainties of these factors are generally denoted as δ_y, which is described as follows [35]:

$$\delta_y = \sqrt{(\frac{\partial y}{\partial x_1}\delta x_1)^2 + (\frac{\partial y}{\partial x_2}\delta x_2)^2 + \cdots + (\frac{\partial y}{\partial x_n}\delta x_n)^2} \tag{10}$$

where δx_1, δx_2, $\ldots\delta x_n$ are the uncertainty of the directly measured values.

The relative uncertainties of Q_{hp}, *COP*, m_{ref}, R_{fcr} and R_{icr} are generally described as follows:

$$\frac{\delta Q_{hp}}{Q_{hp}} = \sqrt{\left(\frac{\delta m_w}{m_w}\right)^2 + 2(\frac{\delta T}{T_{con.out} - T_{con.in}})^2} \tag{11}$$

$$\frac{\delta COP}{COP} = \sqrt{\left(\frac{\delta m_w}{m_w}\right)^2 + 2(\frac{\delta T}{T_{con.out} - T_{con.in}})^2 + \left(\frac{\delta W_{hp}}{W_{hp}}\right)^2} \tag{12}$$

$$\frac{\delta m_{ref}}{m_{ref}} = \sqrt{\left(\frac{\delta m_w}{m_w}\right)^2 + 2(\frac{\delta T}{T_{con.out} - T_{con.in}})^2 + \left(\frac{\delta h}{h_1 - h_2}\right)^2} \tag{13}$$

$$\frac{\delta R_{fcr}}{R_{fcr}} = \sqrt{\left(\frac{\delta P_{epl}}{P_{epl}}\right)^2 + \left(\frac{\delta P_{dp}}{P_{dp}}\right)^2} \tag{14}$$

$$\frac{\delta R_{icr}}{R_{icr}} = \sqrt{\left(\frac{\delta P_{vil}}{P_{vil}}\right)^2 + \left(\frac{\delta P_{dp}}{P_{dp}}\right)^2} \tag{15}$$

5. Results and discussion

In this Section, the simulation results are first presented with some assumptions. Comprehensive experimental data are then provided. The influences of refrigerant charge quantity, opening degree of the throttle valve and flow rate of the exhaust air are investigated. The feasibility of using exhaust air for defrosting is also estimated.

5.1. *Theoretical analysis*

The refrigerant is R410A. The compressor has an efficiency of 0.78. The minimum temperature difference in the heat exchangers and the air temperature drop in the low-pressure evaporator are 5 °C. The vapour injection temperature is 5 °C. The exhaust air has a temperature of 20 °C. The condensation temperature of the refrigerant is 45 °C. The fan power and pressure drop of refrigerant in the heat exchangers are not taken into account.

The COPs of the conventional ASHP, VIHP and novel HRVI-ASHP under different ambient temperatures are displayed in Fig. 11. The COP of the HRVI-ASHP ranges from about 3.64 to 4.07, which increases with the increment in the ambient temperature. It is 3.27 to 3.80 for the VIHP and 2.96 to 3.53 for the ASHP. Obviously, the proposed heat pump has a higher COP and the advantage is more appreciable at a lower ambient temperature. For instance, the relative COP increment of the novel heat pump over the VIHP and ASHP is 11.2% and 22.9% respectively at −10 °C. HRVI-ASHP has two evaporation temperatures: one is the vapour injection temperature (i.e, 5 °C) while the other (about −20 °C) is related to the ambient temperature. The former is higher than the latter by about 25 °C. HRVI-ASHP can be deemed as a combination of a VIHP operating at evaporation temperature of −20 °C and an ASHP operating at evaporation temperature of 5 °C. The COP of an ASHP operating at evaporation temperature of 5 °C is significantly higher than that of ASHP and VIHP operating at evaporation temperature of −20 °C, and the COP of HRVI-ASHP is thereby higher.

The exergy destruction due to the throttling process for the three kinds of heat pumps is depicted in Fig. 12. The vertical axis denotes the ratio of E_d to the compressor power input. E_d per kW power input of the ASHP is much larger than the VIHP and novel heat pump. Compared with a conventional ASHP, HRVI-ASHP can reduce E_d and there are two reasons. Firstly, the refrigerant from the condenser is split into two streams. E_d of the first stream in the medium-pressure throttle valve is weakened due to a higher p_o. Secondly, E_d of the second stream is reduced by a lower v as the refrigerant is supercooled prior to the expansion. The E_d per kW power input of the ASHP at −10 °C is 0.21, which is 2.35 times that of the novel heat pump. The throttling irreversibility of the VIHP is lowest. The reason is that for an ASHP operating at evaporation temperature of 5 °C, the E_d per kW power input is about 0.15, which is still higher than that of the VIHP. As a combination of a VIHP operating at evaporation temperature of −20 °C and an ASHP operating at evaporation temperature of 5 °C, HRVI-ASHP, therefore has larger throttling irreversibility than the VIHP.

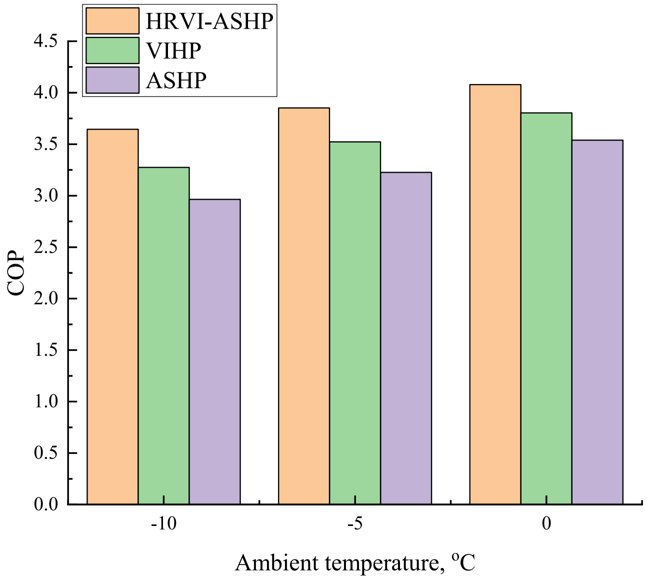

Fig. 11. COP comparison among the conventional ASHP, VIHP and HRVI-ASHP under different ambient temperatures.

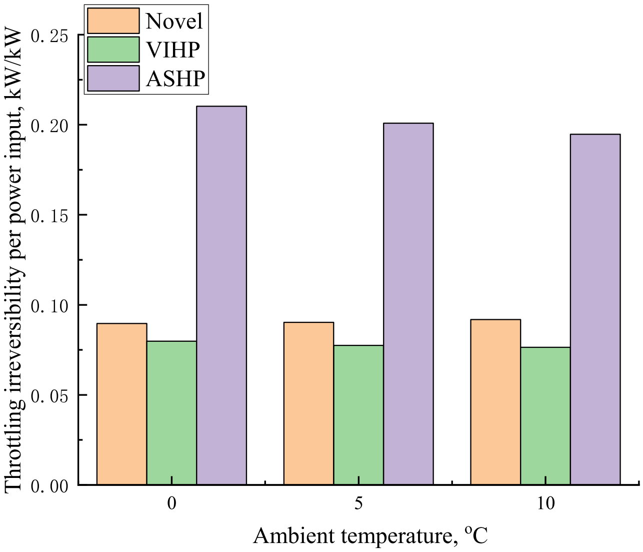

Fig. 12. Thermodynamic irreversibility related to throttle valves for ASHP, VIHP and HRVI-ASHP under different ambient temperatures.

Compared with the VIHP, HRVI-ASHP has an additional evaporator, which is heated by the exhaust air. The mass ratio of the injected refrigerant to the non-injected refrigerant is increased. The average evaporation temperature is higher than that of both ASHP and VIHP, leading to a lower compressor power input. Fig. 13 shows the power

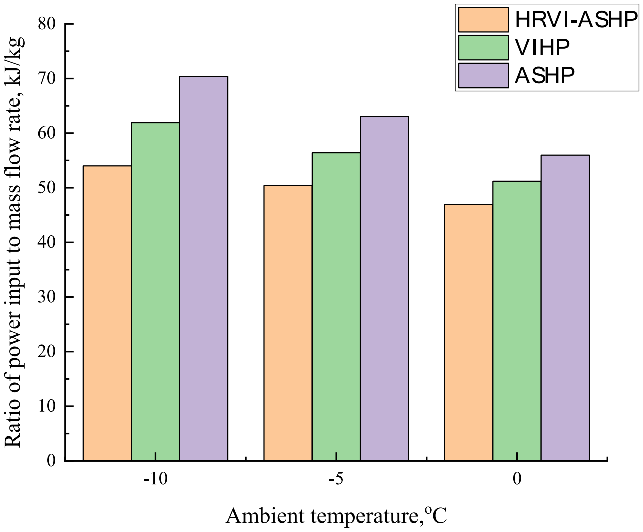

Fig. 13. Ratio of compressor power consumption to refrigerant mass flow rate for ASHP, VIHP and HRVI-ASHP under different ambient temperatures.

input per kg of refrigerant. Given the mass flow rate at the compressor outlet, the power consumption of HRVI-ASHP is the lowest. For example, it is 54.0 kJ/kg at −10 °C, compared to 61.9 kJ/kg and 70.4 kJ/kg for the VIHP and ASHP.

5.2. *Experimental investigation*

The experiment was conducted in four aspects that can influence the performance of an HRVI-ASHP, including refrigerant charging quantity, EEVs apertures, volume flow rate of the exhaust air and defrosting time.

5.2.1. *Refrigerant charging quantity*

The experiment was started to optimize the refrigerant charging quantity. The tests were conducted in the standard conditions, i.e., temperature 0 °C and pressure 101 kPa in the laboratory. The exhaust air from the laboratory outside had a temperature of 24 °C. The apertures of the two EEVs in the vapour injection line and the evaporation line were 32% and 24%, respectively. The refrigerant charging quantity increased from 1 to 3.04 kg. The experimental results of the relevant parameters in the water tank circuit, including the condenser inlet temperature, the condenser outlet temperature, and the volume flow rate are listed in Table 3. Along with the increase of the refrigerant charging quantity, the volume flow rate and the condenser inlet temperature remained stable.

As shown in Fig. 14, an increase of the refrigerant charging quantity led to a decrement in the power consumption from 2800 W to 2500 W. However, the generated heat from the HRVI-ASHP increased gradually from 4500 W to 6100 W and remained constant after the refrigerant charging quantity reached 2.7 kg. The decrease of the power and the increase of the generated heat resulted in an overall improvement of the HRVI-ASHP performance.

Based on the variations of the power and generated heat, the COP of the heat pump is calculated and shown in Fig. 15. The COP was relatively low as compared to those in Sections 5.2.2 and 5.2.3. The reason is that the refrigerant quantity was adjusted under apertures of the two EEVs of 32% and 24%. The EEV apertures were not optimal. The COP increased gradually with the increasing refrigerant charging quantity and peaked at 2.5 when the charging quantity reached 2.7 kg. When the charging quantity passed 2.7 kg, the COP of the heat pump remained around 2.5. Hence, the optimal refrigerant charging quantity of the heat pump was identified as 2.7 kg.

The experimental results for the relevant parameters in the heat pump compression circuit, including the condensing pressure, the condensing temperature, the evaporating pressure, the evaporating temperature, and the vapour injection pressure, are shown in Table 4. As the refrigerant charging quantity was increased, the condensing, evaporating, and vapour injection pressures initially experienced a decrease followed by an increase. In addition, the condensing temperature decreased gradually whilst the evaporating temperature increased.

Fig. 16 shows the variation of the final compression ratio as well as the evaporation temperature in the evaporation line along with the refrigerant charging quantity. The final compression ratio decreased from 4 to 2.6 while the refrigerant charging quantity increased from 1 kg to 3 kg. The decline of the final compression ratio was accompanied by an increase in the evaporation temperature of the heat pump which increased from −11 °C to −4°C. Accordingly, the increase of the refrigerant mass flow rate, the decrease of the final compression ratio and the increase of the evaporation temperature contributed to the improvement of the heat pump performance.

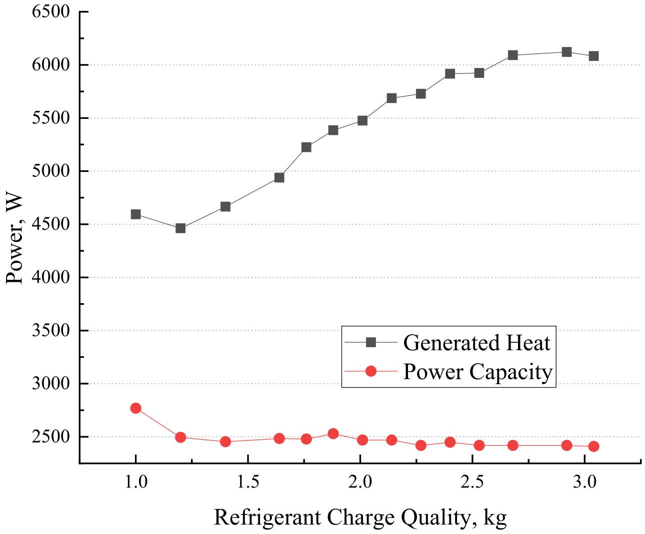

Fig. 14. Variation of the power and the heat supply with the refrigerant charge quantity.

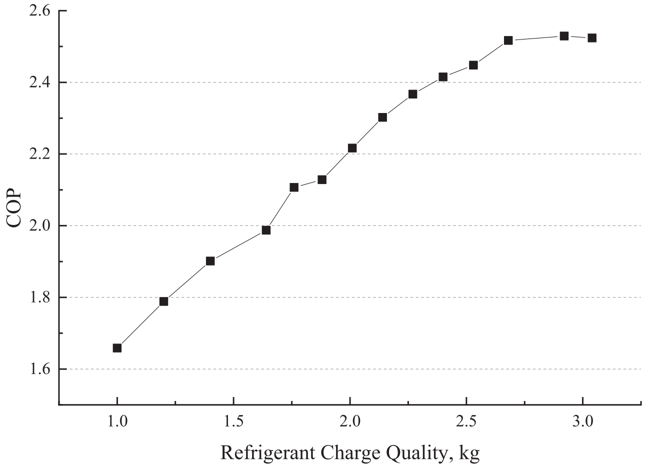

Fig. 15. Variation of the COP with the refrigerant charge quantity.

5.2.2. *Apertures of the expansion valves*

After finding the optimal refrigerant charging quantity, the apertures of the two EEVs in the vapour injection line and the evaporation line were adjusted to test the performance of the HRVI-ASHP under the standard test conditions. For simplicity, the aperture of the EEV in the vapour injection line will be called the vapour injection line aperture (VILA), and the aperture of the EEV in the evaporation line will be called the evaporation line aperture (ELA). The experimental results for the

Table 3
Waterside and the increasing refrigerant charging quantity.

Refrigerant charging quantity (kg)	1	1.2	1.4	1.64	1.76	1.88	2.01
Condenser inlet temperature (°C)	31.6	27.2	26.0	25.6	25.5	25.5	25.1
Condenser outlet temperature (°C)	34.7	30.0	28.9	28.7	28.8	28.9	28.6
Volume flow rate (m^3/h)	1.27	1.36	1.36	1.36	1.37	1.36	1.34
Refrigerant charging quantity (kg)	2.14	2.27	2.4	2.53	2.68	2.917	3.037
Condenser inlet temperature (°C)	25.2	25.3	25.4	25.4	25.5	25.4	25.4
Condenser outlet temperature (°C)	28.8	28.9	29.2	29.2	29.4	29.4	29.3
Volume flow rate (m^3/h)	1.34	1.34	1.34	1.34	1.34	1.34	1.34

Table 4
Variation of heat pump circulation parameters with increasing refrigerant charging quantity on refrigerant side.

Refrigerant charging quantity (kg)	1	1.2	1.4	1.64	1.76	1.88	2.01
Condenser inlet pressure (MPa)	2.169	1.868	1.83	1.822	1.838	1.845	1.849
Evaporator inlet pressure (MPa)	0.563	0.551	0.579	0.604	0.626	0.633	0.641
Evaporator inlet temperature (°C)	−11.5	−11.49	−11.02	−9.79	−8.73	−8.37	−7.82
Refrigerant charging quantity (kg)	2.14	2.27	2.4	2.53	2.68	2.917	3.037
Condenser inlet pressure (MPa)	1.86	1.864	1.882	1.89	1.899	1.902	1.902
Evaporator inlet pressure (MPa)	0.659	0.67	0.687	0.702	0.709	0.723	0.73
Evaporator inlet temperature (°C)	−7	−6.56	−5.85	−5.19	−4.97	−4.28	−4.07

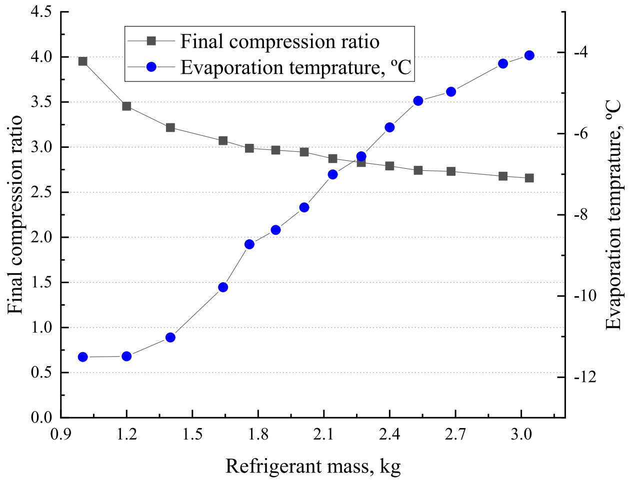

Fig. 16. Variation of the compression ratio with respect to the charge quantity.

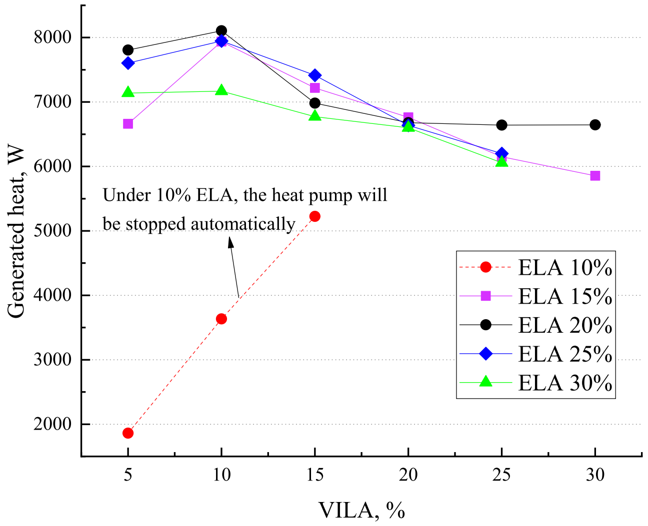

Fig. 17. Variation of the generated heat with EEVs' aperture.

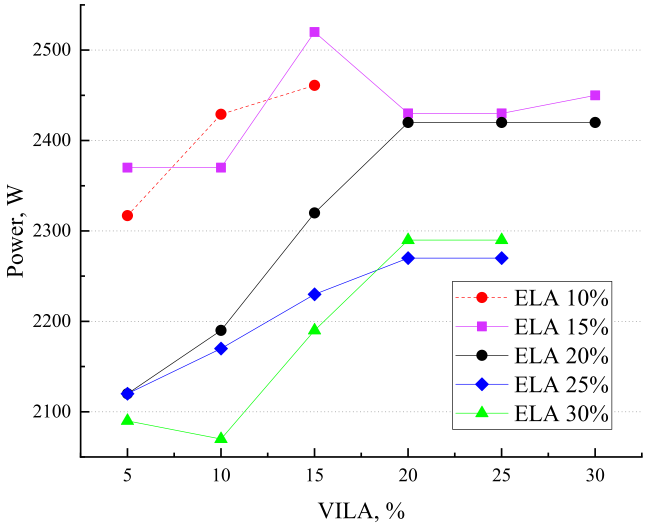

Fig. 18. Variation of the power input with EEVs' aperture.

relevant parameters in the water tank circuit, including the condenser inlet temperature, the condenser outlet temperature, and the volume flow rate, are shown in Table 5.

The variations of the generated heat and the power along with the different apertures of the two EEVs are shown in Fig. 17 and Fig. 18, respectively. The separate lines in these figures represent variations for different ELAs. Given an ELA, the heat supply and power consumption varied with the VILA, thus forming the operation points with different apertures of both EEVs.

As shown in Fig. 17, when ELA reached 10%, the refrigerant mass flow rate was seriously limited by the small aperture, and the compressor could not receive enough refrigerant, thus causing the compressor not to operate properly. Consequently, the self-protection program of the heat pump was activated and the heat pump was shut down automatically. Under other ELAs from 15% to 25%, the generated heat was increased when VILA varied from 5% to 10% and peaked at 10%. Then, the generated heat decreased when VILA increased from 10% to 30%. The generated heat first raised and then descended mainly because the refrigerant mass flow rate in the vapour injection line increased with the increase of VILA. From 5% to 10% VILA, the increased mass flow rate in the vapour injection line can benefit the heat transfer, thus enhancing the generated heat. However, the continuous growth of the refrigerant mass flow rate in the vapour injection line eventually surpasses the line's heat transfer capacity, thereby leading to incomplete vaporization of the refrigerant. In addition, under 10% VILA,

Table 5
Waterside along with the variation of the EEV's aperture.

ELA	VILA	Condenser inlet temperature (°C)	Condenser outlet temperature (°C)	Volume flow rate (m^3/h)
15%	5%	25.47	29.67	1.36
	10%	25.48	30.48	1.36
	15%	25.77	30.39	1.34
	20%	25.56	29.73	1.39
20%	5%	25.57	30.49	1.36
	10%	25.62	30.73	1.36
	15%	25.64	30.04	1.36
	20%	25.68	29.86	1.37
25%	5%	25.2	29.89	1.39
	10%	25.16	30.06	1.39
	15%	25.15	29.68	1.4
	20%	25.27	29.36	1.39
30%	5%	25.31	29.71	1.39
	10%	25.33	29.75	1.39
	15%	25.34	29.52	1.39
	20%	25.35	29.42	1.39

when ELA increased from 15% to 30%, the generated heat decreased drastically. The analysis revealed that under 10% VILA and 15% ELA conditions, the heat pump generated maximum heat.

As shown in Fig. 18, when ELA increased from 15% to 25%, the power capacities increased with the increase of VILA. After VILA peaked at 15% or 20%, the power capacities dropped or remained constant. Furthermore, when ELA was 30%, the power decreased firstly and then increased after 10% VILA, then remained constant after the VILA reached 20%. According to the analysis, the 10% VILA and 30% ELA lead to the lowest energy consumption of the HRVI-ASHP.

Based on the generated heat and the power of the HRVI-ASHP, the COP was calculated and is shown in Fig. 19. When ELA increased from 15% to 30%, the COP of the HRVI-ASHP increased slightly with the increase of VILA from 5% to 10%. Then, the COP dropped with an increase of VILA. Consequently, the heat pump with 10% VILA and 20% ELA reached the highest COP. The analysis showed that the main factor influencing the COP of the heat pump was the generated heat.

The experimental results for the relevant parameters in the heat pump circuit, including the condensing pressure, evaporating pressure, evaporating temperature, and vapour injection pressure, are shown in Table 6. With the increase of the ELA, the condensing pressure and the evaporating pressure under the same VILA showed an increasing trend.

Furthermore, the final compression ratio can also reflect the performance of the heat pump. Fig. 20 shows the variation of the final compression ratio with respect to the EEVs' apertures. Under each ELA, the final compression ratio bottomed at the lowest value under 10% VILA, which can explain why the heat pump can operate better under 10% VILA compared to other apertures. When it comes to ELA, the final compression ratio reached the highest under 15% ELA. The excessive final compression ratio led to an unfavourable effect on the performance of the heat pump and thus a lower COP. Under 20% ELA, the lowest final compression ratio was also achieved at 10% VILA. The fluctuation range of the final compression ratio was low and the value of it remained around 2.7. Under the ELAs of 25% and 30%, the final compression ratio was around 2.5.

Fig. 21 shows the variation of intermediate compression ratio with respect to the variation of the EEVs apertures. Similar to the variation of the final intermediate compression ratio, the intermediate compression ratio reached the highest value when the aperture of the ELA was 15%, which was detrimental to the heat pump performance. Along with the increase of VILA, the intermediate compression ratios under different ELAs showed similar variation trends and decreased gradually.

Fig. 22 shows the evaporation temperature varied along with the variation of the EEVs' apertures. It is seen that the highest evaporation temperatures appeared when VILA reached 10%. In addition, with the increase of ELA, the evaporation temperature increased, which means the higher ELAs can help reduce the final compression ratio and indirectly increase the performance of the heat pump.

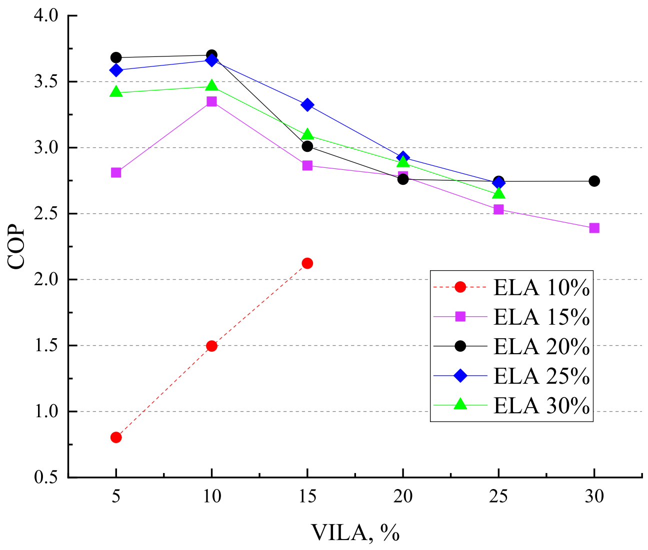

Fig. 19. Variation of the COP with EEVs' aperture.

Table 6
Heat pump circuit parameters along with the variation of the EEV's aperture on refrigerant side.

ELA	VILA	Condenser inlet pressure (MPa)	Evaporator inlet pressure (MPa)	Evaporator inlet temperature (°C)	Vapour injection pressure (MPa)
15%	5%	3.058	0.583	−10.69	1.10
	10%	2.166	0.676	−6.16	1.15
	15%	2.036	0.465	−16.03	1.30
	20%	1.942	0.474	−16.61	1.44
20%	5%	2.053	0.801	−3.18	1.26
	10%	2.006	0.759	−2.91	1.30
	15%	1.923	0.692	−5.66	1.53
	20%	1.918	0.693	−5.66	1.64
25%	5%	1.959	0.799	−1.20	1.27
	10%	1.968	0.809	−0.85	1.34
	15%	1.940	0.770	−2.27	1.40
	20%	1.894	0.693	−5.34	1.49
30%	5%	1.944	0.803	−1.04	1.26
	10%	1.946	0.806	−0.94	1.26
	15%	1.921	0.782	−1.85	1.42
	20%	1.956	0.736	−3.61	1.55

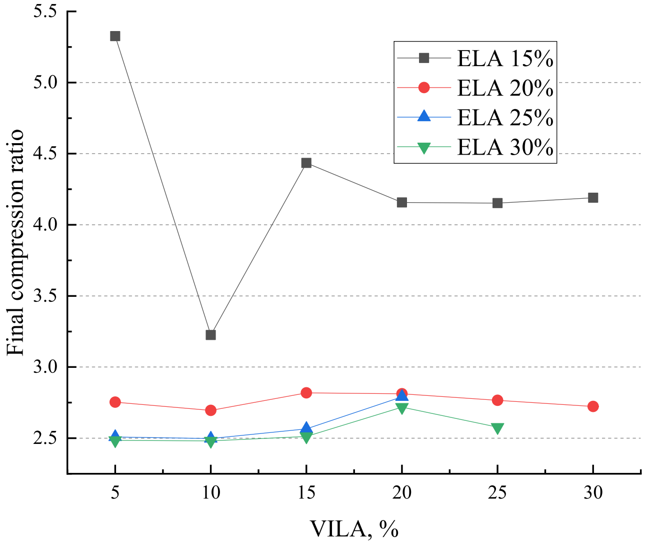

Fig. 20. Variation of the final compression ratio with respect to EEVs aperture.

5.2.3. *Volume flow rate of the exhaust air*

The performance of the heat pump is also affected by the air volume flow rate of the exhaust air. This can greatly influence the available heat of the exhaust air and the evaporation temperature of the evaporator in the evaporation line. In order to simulate a real winter ambient environment, the laboratory temperature was set to 4 individual temperature points from −5°C to 10 °C with a 5 °C interval. The experimental results for the relevant parameters in the water tank circuit are shown in Table 7, including the condenser inlet temperature, the condenser outlet temperature, and the volume flow rate. When the exhaust airflow rate varied, the volume flow rate of the water tank circuit and the condenser inlet temperature remained stable. Under different ambient temperatures, the condenser outlet temperature increased with the increment in the exhaust air volume flow rate.

Given the pre-set laboratory temperature, the generated heat varied

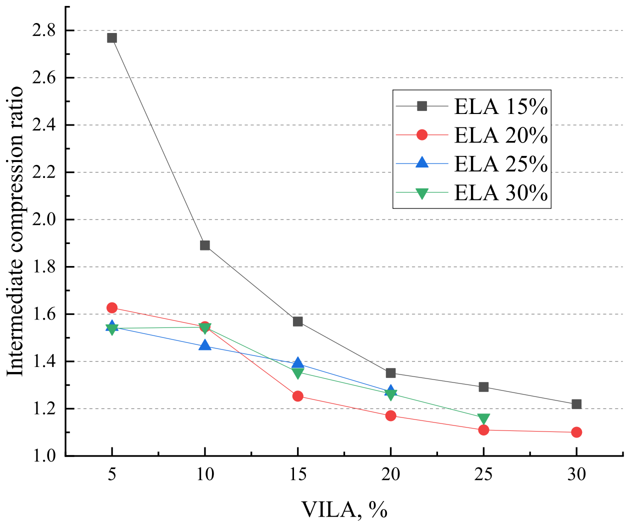

Fig. 21. Variation of the intermediate compression ratio with respect to EEVs apertures.

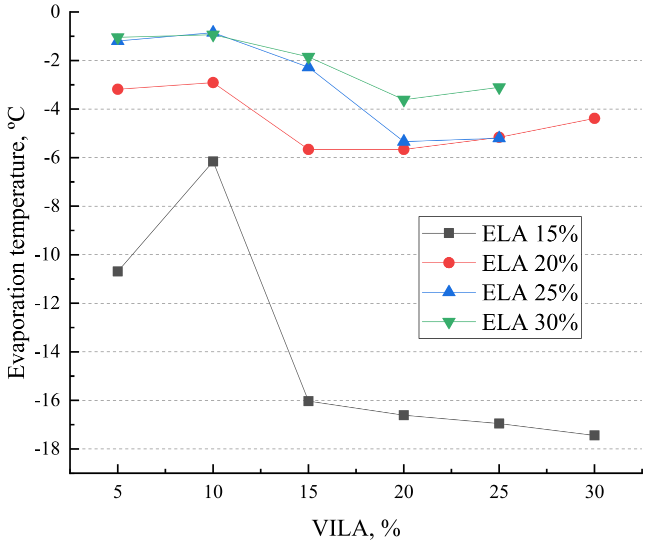

Fig. 22. Variation of the evaporation temperature with respect to EEVs apertures.

with the exhaust air volume flow rate, as shown in Fig. 23. The variations of the generated heat under different laboratory temperatures showed the same trend. The heat supply increased with the increase of the exhaust airflow rate. When the exhaust airflow rate reached 1584 m^3/h, the heat remained almost constant.

Fig. 24 shows the variation of the power with the exhaust airflow rate. Unlike the generated heat, the variation of the power of the heat pump had no uniform pattern which was mainly due to the mechanical characteristics of the compressor. However, under different ambient temperatures, the absolute variations of the power were very small, from 10 W to 130 W. Hence, the exhaust airflow had a minor impact on the power input of the heat pump.

As shown in Fig. 25, the variation of COP of the heat pump was similar to that of the generated heat. Under different ambient temperatures, the COP increased with the rise of the airflow rate. Once the exhaust airflow rate reached 1584 m^3/h, the COP increment slowed down and remained stable. This means that the heat pump can make full use of the heat from the exhaust air when the exhaust airflow rate reaches 1584 m^3/h, and the additional spare heat was wasted when the

Table 7
Waterside parameters at the different exhaust air volume flow rates.

Ambient temperature (°C)	Exhaust air volume flow rate (m^3/h)	Condenser inlet temperature (°C)	Condenser outlet temperature (°C)	Volume flow rate of condenser (m^3/h)
−5	367.2	24.21	27.86	1.43
	734.4	24.20	28.05	1.43
	1224	24.21	28.29	1.43
	1591.2	24.22	29.02	1.43
0	367.2	24.22	28.28	1.43
	734.4	24.21	28.48	1.43
	1224	24.25	29.01	1.43
	1591.2	24.26	29.34	1.43
5	367.2	24.39	29.15	1.43
	734.4	24.40	29.38	1.43
	1224	24.42	29.67	1.43
	1591.2	24.43	29.92	1.43
10	367.2	24.58	29.94	1.42
	734.4	24.57	30.22	1.42
	1224	24.58	30.32	1.42
	1591.2	24.58	30.53	1.42

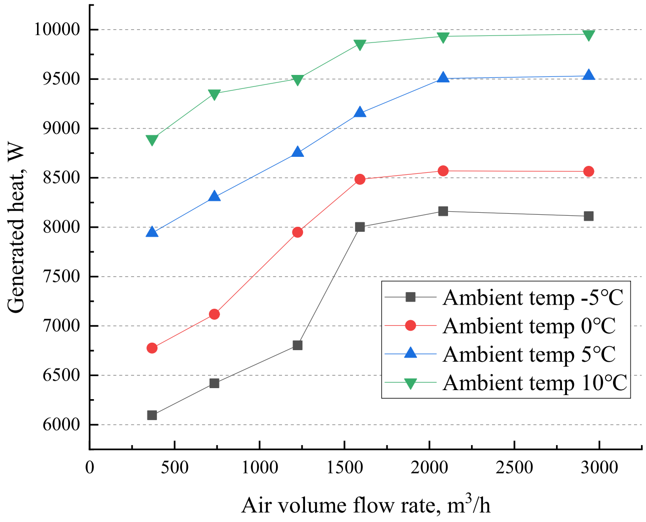

Fig. 23. Variation of the generated heat with exhaust air volume flow rate.

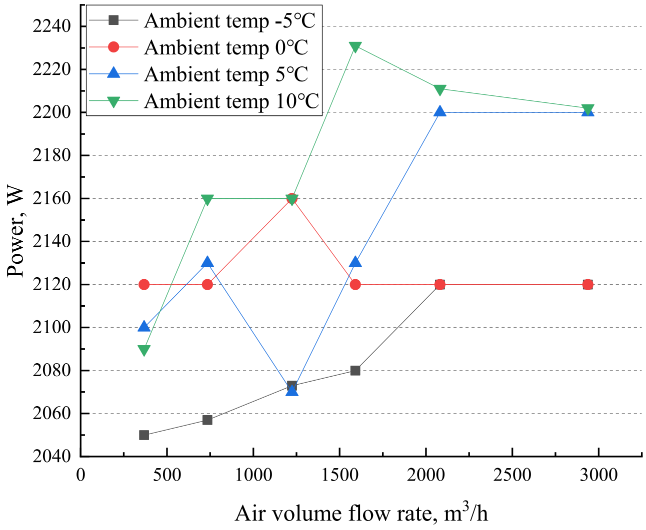

Fig. 24. Variation of the power with exhaust air volume flow rate.

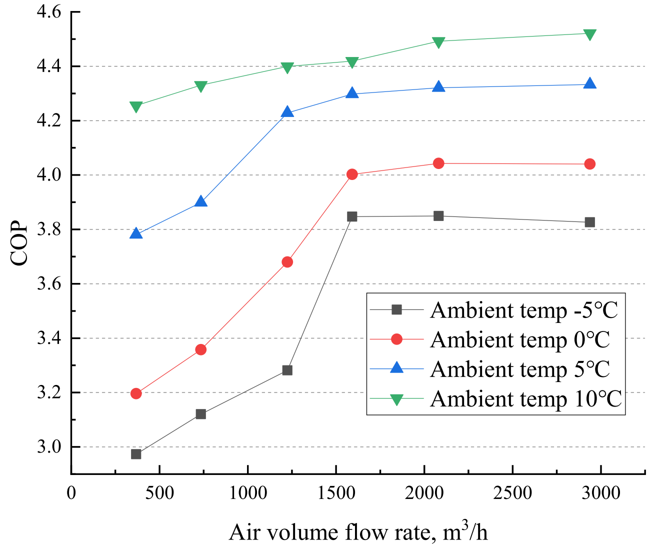

Fig. 25. Variation of the COP with exhaust air volume flow rate.

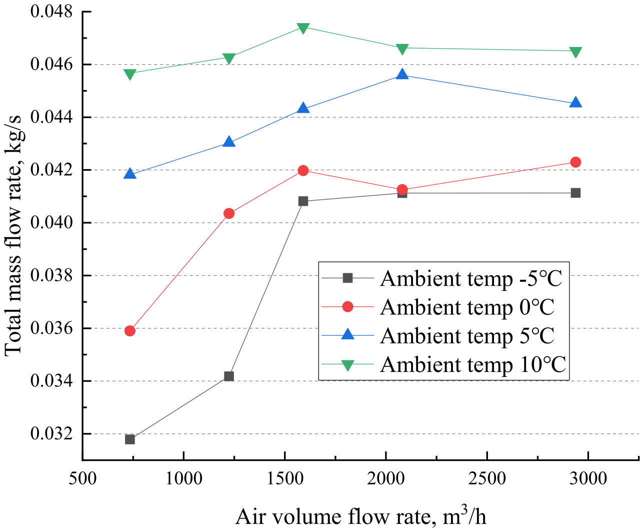

Fig. 26. Variation of the total refrigerant mass flow rate with exhaust air volume flow rate.

exhaust airflow rate surpassed this level. The experimental results for the relevant parameters in the heat pump circuit are shown in Table 8. With the increase of the exhaust air volume flow rate, the condensing, evaporating, and vapour injection pressures all increased.

As shown in Fig. 26, the variation trend of the total refrigerant mass flow rate was similar to that of the COP and increased with the growth of the exhaust airflow rate up to 1584 m^3/h. Once the volume flow rate passed 1584 m^3/h, the total refrigerant mass flow rate remained constant. The ambient temperature was another factor influencing the total refrigerant mass flow rate. A lower the ambient temperature resulted in a lower the total refrigerant mass flow rate. This relationship was more obvious when the exhaust airflow rate was low. The difference between the total refrigerant mass flow rates under different ambient temperatures became smaller when the exhaust air volume flow rate increased.

Fig. 27 shows the final compression ratio variation with the exhaust air volume flow rate. For ambient temperatures from −5°C to 5 °C, it decreased when the exhaust airflow rate increased from 367 m^3/h to 1584 m^3/h, and the variation for the final compression ratio was more significant under lower temperatures. After the exhaust air volume flow rate passed 1584 m^3/h, the final compression ratio remained stable.

Fig. 28 shows that the intermediate compression ratio had a similar variation to the final compression ratio. At ambient temperatures from −5°C to 5 °C, it decreased when the exhaust air volume flow rate increased from 367 m^3/h to 1584 m^3/h. After the exhaust air volume

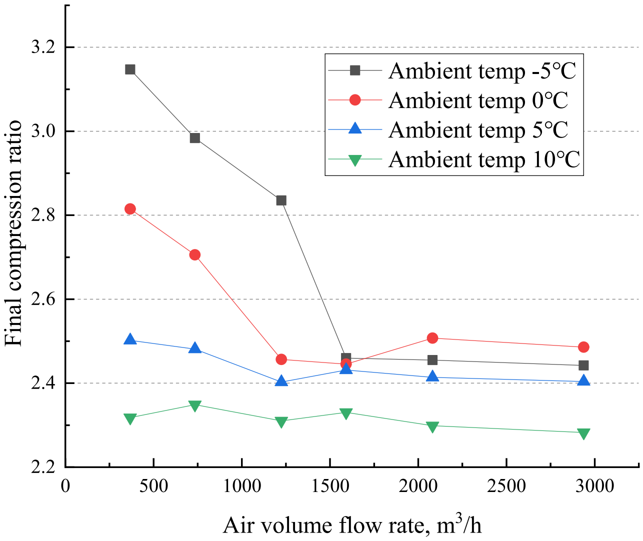

Fig. 27. Variation of the final compression ratio with exhaust air volume flow rate.

Table 8
Heat pump circulation parameters along with the variation of the exhaust air volume flow rate on refrigerant side.

Ambient temperature (°C)	Exhaust air volume flow rate (m^3/h)	Condenser inlet pressure (MPa)	Evaporator inlet pressure (MPa)	Evaporator inlet temperature (°C)	Vapour injection pressure (MPa)
−5	367.2	1.838	0.598	−9.95	0.952
	734.4	1.851	0.637	−8.09	1.003
	1224	1.869	0.677	−6.33	1.060
	1591.2	1.919	0.797	−1.40	1.245
0	367.2	1.868	0.680	−5.98	1.071
	734.4	1.881	0.711	−4.67	1.120
	1224	1.917	0.796	−1.18	1.249
	1591.2	1.968	0.820	−0.31	1.287
5	367.2	1.920	0.784	−1.40	1.237
	734.4	1.944	0.801	−0.68	1.282
	1224	1.978	0.838	0.66	1.323
	1591.2	2.070	0.867	1.69	1.368
10	367.2	1.974	0.867	1.63	1.373
	734.4	2.035	0.882	2.23	1.429
	1224	2.062	0.907	3.11	1.437
	1591.2	2.151	0.937	4.23	1.478

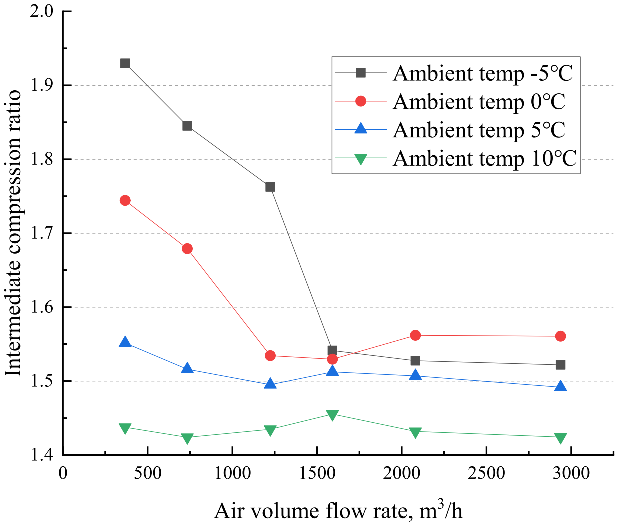

Fig. 28. Variation of the intermediate compression ratio with exhaust air volume flow rate.

flow rate passed 1584 m^3/h, the intermediate compression ratio was almost constant. Besides, the ambient airflow rate of HRVI-AHSP was 6000 m^3/h and therefore the mass flow ratio of the ambient inlet air and the exhaust air in the test ranged from 3.8 to 16.3.

5.2.4. *Defrosting process*

The quick and efficient defrosting process is an important advantage of the proposed HRVI-ASHP. Frosting on the evaporator surface can be removed quickly by using exhaust air from the building, during which the heat pump can be turned off and thus reduce the energy consumption of the compressor. Two defrosting processes carried out on the 16th and 17th of November 2019 are presented in this paper. The power variation of the heat pump during the defrosting processes is shown in Fig. 29 and Fig. 30, respectively. On the 16th of November, the power dropped to 0 W during the defrosting process as the exhaust air extracted from the building was used to defrost the ice. The exhaust air was extracted by a ventilation system with high temperature and then sent to the heat pump evaporators directly to defrost the ice. After 4mins of the defrosting process, the heat pump commenced operation and took 7mins to get back to the normal operation. In the start-up stage, the power increased to 1800 W, then it fluctuated from 1800 W to 2300 W before eventually settling at around 2400 W. Similar to the defrosting process on the 16th of November, the defrosting process on the 17th of November took 4mins for defrosting and 3mins for start-up respectively. The short defrosting time demonstrated the effectiveness of the novel HRVI-ASHP using the exhaust air.

The variations of the evaporator temperature and COP during the defrosting processes were also monitored and are presented in Figs. 31 and 32. During the defrosting period, the evaporator temperature increased rapidly due to the high temperature of the exhaust air. To defrost the heat pump completely, the minimum defrosting time is 4mins. The compressor operated when the temperature difference between the evaporator surface and the exhaust air was below 20 °C. On the 16th of November, after the defrosting, the heat pump restarted. Initially, the evaporator temperature remained at around 4 °C because the compressor had a gradual start, thus leading to a gradual increase of COP. Along with the increasing COP, the evaporator temperature fell to −12 °C due to the low refrigerant mass flow rate. After 15:35, the compressor returned to normal operation gradually. As the COP and the refrigerant mass flow rate increased, the evaporator temperature also increased until it reached −5.5 °C. On the 17th of November, the evaporator temperature increased rapidly during the defrosting period and remained around 5 °C in the start-up stage. The evaporator temperature fell down over the next two minutes and then bounced back as when the heat pump returned to the normal operation.

5.2.5. *Uncertainty analysis*

The relative uncertainties of the generated heat (Q_{hp}), the coefficient of performance (*COP*), the total refrigerant mass flow rate (m_{ref}), the final compression ratio (R_{fcr}), and the intermediate compression ratio (R_{icr}) are determined by using the Pythagorean summation of discrete uncertainties with a confidence interval of 95% [36]. According to Eq.9 to Eq.13, the uncertainties of the evaluated values are shown in Table 9. According to the derived uncertainty values, the results of the evaluated values are satisfactory for this study.

5.3. *Comparison between the simulation results and experiment data*

Given the simulation results and experiment data in Sections 5.1 and 5.2, a comparison between the predicted and actual COP of the heat pump is made in Fig. 33. The ambient temperature is −5, 0, 5 and 10 °C, respectively. The condenser's outlet temperature is about 35 °C. The mass flow ratio of the ambient air to the exhaust air is 4.0. It is obvious

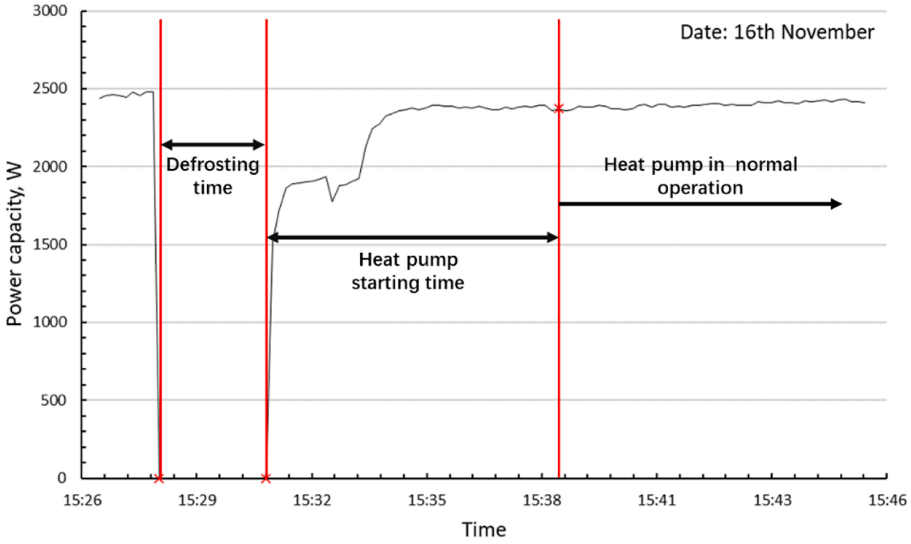

Fig. 29. Heat pump power for the defrosting process on the 16th November.

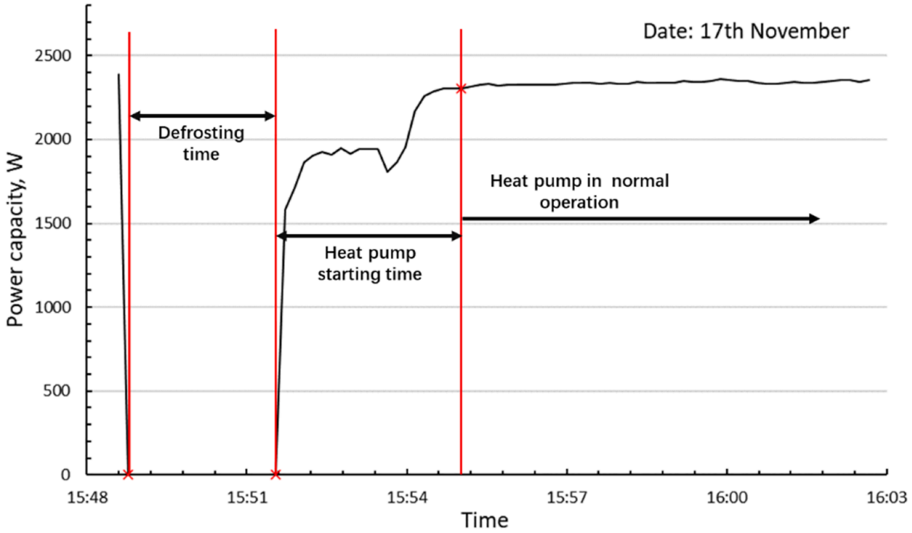

Fig. 30. Heat pump power in the defrosting process on the 17th November.

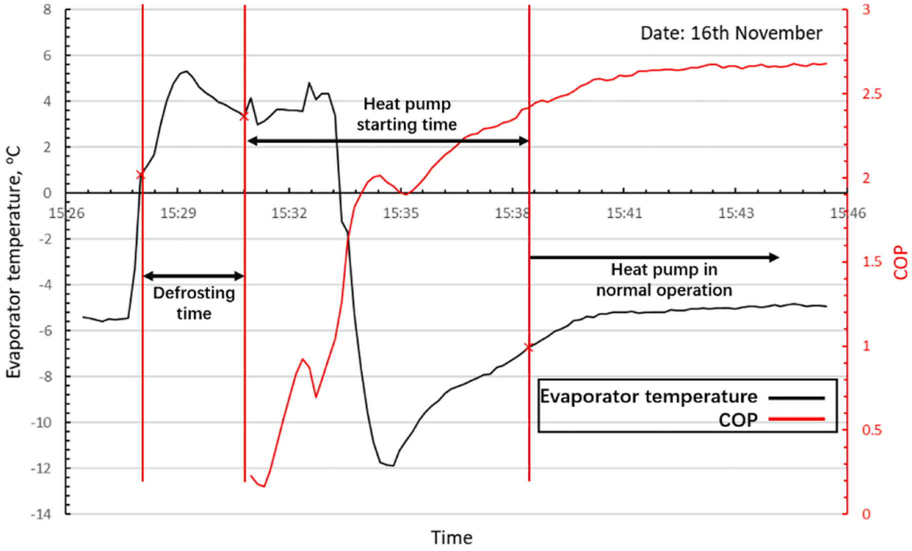

Fig. 31. Heat pump evaporator temperature and the COP on the 16th November.

that the actual COP is lower than the simulation result. For example, at the ambient temperature of −5 °C, the actual COP is 23% less than the simulated value. The main reason is that the simulation is carried out at a constant compressor efficiency of 78%. In practice the working conditions of the compressor may deviate from the design conditions, leading to the part-load operation with a lower compressor efficiency. Besides the actual COP has taken all the power consumption into account while in the simulation the fan/pump power is neglected.

The prototype has a lower COP than predicted since it is first-of-its-kind and not much lesson could be learned from experience. Nevertheless, the technical feasibility of the prototype has been demonstrated by the experimental tests, and the defrosting approach using ventilation air is fast and efficient. In the future, the COP of the novel heat pump will be further elevated if the vapour injection (VI) compressor is designed and manufactured for the waste heat recovery purpose. At present, a conventional VI compressor has been employed in the prototype, which is not meant to be used for the ventilation waste recovery. Though in theory the vapour injection rate can be increased as more refrigerant is vaporized in the vapour injection line, in practice the increment might not be appreciable for the given structure of the compressor. To explore the potential of the novel heat pump, improvements on the design and manufacture of the VI compressor shall be made in the future.

5.4. Economic analysis

Compared with a conventional VIHP, the novel HRVI-ASHP only adds one more evaporator on the vapour injection line, and thus the cost of an HRVI-ASHP is just about 120 dollars more than that of a conventional VIHP, according to the manufacturer of the prototype.

Take Beijing as an example. The heating load per square meter is about 60 W/m^2 [37]. The heating season is usually from November to March next year. The total heating time is about 3600 h. Accordingly, for a 100 m^2 house, the annual energy demand for space heating is 21600kWh. In Beijing, the average ambient temperature between November and March is −6.9 °C [37]. According to Fig. 11, the average COP of a conventional VIHP is 3.4, and the electricity consumption is 6353kWh for an underfloor heating system. In accordance with the simulation result, the COP of the HRVI-ASHP is 0.3 higher than the conventional VIHP at −6.9 °C, which means the novel HRVI-ASHP only needs to consume 5838kWh electricity for heating the house, thus

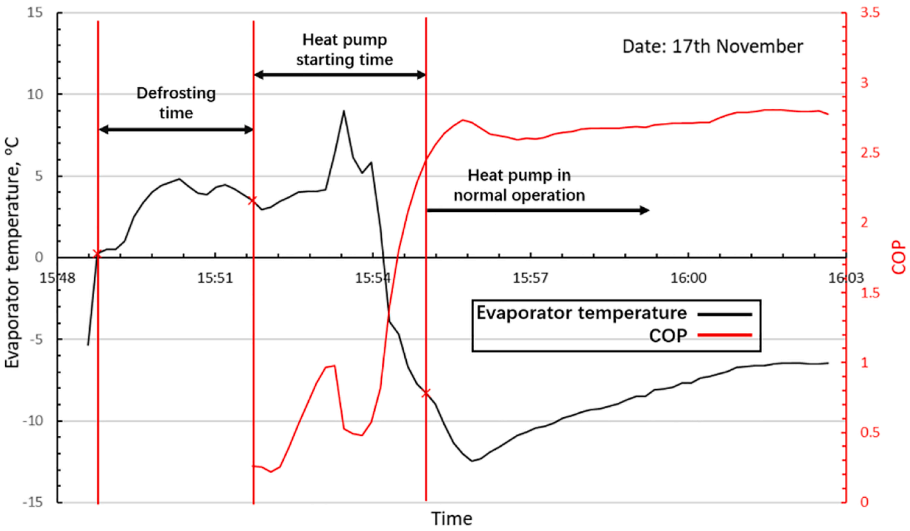

Fig. 32. Heat pump evaporator temperature and the COP on the 17th November.

Table 9
The uncertainties of the evaluated values.

Parameter	Uncertainty	Absolute Error
Q_{hp}	4.3%	±0.09 kW
COP	4.3%	±0.21
m_{ref}	5%	±0.002 kg/s
R_{fcr}	3%	±0.07
R_{icr}	3.5%	±0.1

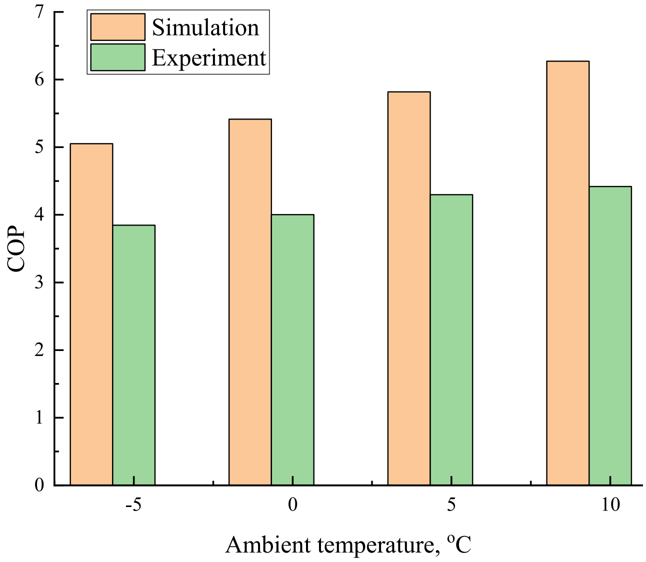

Fig. 33. COP comparison between simulation and experiment.

saving 515kWh compared with the conventional VIHP. Given the electricity price of 0.1dollar/kWh in Beijing, a saving of 51.5 dollars per year can be made by the HRVI-ASHP. As a result, the HRVI-ASHP takes 2.3 years to get the money back for the additional capital cost. Particularly, the HRVI-ASHP tackles the challenge of a conventional VIHP by using exhaust air for defrosting. This will lead to more electricity saving per year and a significantly shorter payback time.

6. Conclusion

This paper proposed a novel dual-source heat recovery vapour injection air source heat pump (HRVI-ASHP) with two evaporators. The vapour injection compressor contains two suction nozzles which are connected with the intermediate-pressure side (vapour injection line) and low-pressure side (evaporation line) separately. The key findings in this study are as follows.

1. The proof-of-concept heat pump prototype has been successfully operating. The HRVI-ASHP has an additional evaporator in the vapour injection line. The newly designed structure of the HRVI-ASHP uses exhaust air as part of the heat source, thus overcoming the restriction of a limited heating capacity of the conventional exhaust air heat pump.
2. The performance of the prototype was influenced by the refrigerant charging quantity, opening degree of throttle valves, and flow rate of exhaust air. The optimal refrigerant charging quantity was about 2.7 kg. Given the opening degree of the throttle valve in the vapour injection line, there was an optimum opening degree of the valve in the evaporation line. When the apertures of the throttle valves in vapour injection line in the evaporation line were 20% and 10%, the heat supply and COP of the heat pump peaked at 8.3 kW and 3.65. The heat supply and COP increased with an increment in the exhaust air flow rate. However, the increment was slight when the flow rate exceeded 1584 m^3/h.
3. The exhaust air can directly drive the defrosting process. According to the experiment results, the defrosting process of the HRVI-ASHP was just 4mins with negligible power consumption, which was quick and energy efficient. The unique defrosting approach can tackle the challenge of a conventional air source heat pump and vapour injection heat pump in the cold climate area application.
4. Further improvement of the prototype is needed. In particular, the mainstream vapour injection compressors on the market use ambient air as the heat source and are not designed for waste heat recovery purposes. For better performance of the HRVI-ASHP, the design and manufacture of the compressor shall be improved to allow a larger vapour injection rate in operation.

CRediT authorship contribution statement

Yi Fan: Data curation, Formal analysis, Investigation, Validation, Writing – original draft. **Jing Li:** Conceptualization, Methodology, Formal analysis, Software, Writing – original draft. **Xudong Zhao:** Funding acquisition, Supervision, Resources, Writing – review & editing. **Steve Myers:** Writing – review & editing. **Yuanda Cheng:** Writing – review & editing. **Min Yu:** Visualization. **Yousef Golizadeh Akhlaghi:** Software. **Xiaoli Ma:** Resources, Writing – review & editing. **Sen Yu:** Software.

Declaration of Competing Interest

The authors declare that they have no known competing financial interests or personal relationships that could have appeared to influence the work reported in this paper.

Acknowledgements

The authors would like to acknowledge our appreciation for the financial support received from the following projects: 'A low carbon heating system for existing public buildings employing a highly innovative multiple-throughout-flowing micro-channel solar-panel-array and a novel mixed indoor/outdoor air source heat pump' funded by the UK BEIS.

References

[1] Zhang H, Zhao H, Li Z. Waste heat recovery and water-saving modification for a water-cooled gas-steam combined cycle cogeneration system with absorption heat pump. Energy Convers Manage 2019;180:1129–38.

[2] Iruela JRS, Ruiz LGB, Pegalajar MC, Capel MI. A parallel solution with GPU technology to predict energy consumption in spatially distributed buildings using evolutionary optimization and artificial neural networks. Energy Convers Manage 2020;207:112535.

[3] Rastogi M, Chauhan A, Vaish R, Kishan A. Selection and performance assessment of Phase Change Materials for heating, ventilation and air-conditioning applications. Energy Convers Manage 2015;89:260–9.

[4] Liu Z, Li W, Zhang L, Wu Z, Luo Y. Experimental study and performance analysis of solar-driven exhaust air thermoelectric heat pump recovery system. Energy Build 2019;186:46–55.

[5] Kong X, Xi C, Li H, Lin Z. Multi-parameter performance optimization for whole year operation of stratum ventilation in offices. Appl Energy 2020;268:114966.

[6] Chenari B, Dias Carrilho J, Gameiro da Silva M. Towards sustainable, energy-efficient and healthy ventilation strategies in buildings: A review. Renew Sustain Energy Rev 2016;59:1426–47.

[7] Asasian-Kolur N, Sharifian S, Haddadi B, Pourhoseinian M, Mousazadeh Shekarbaghani Z, Harasek M. Membrane-based enthalpy exchangers for coincident sensible and latent heat recovery. Energy Convers Manage 2022;253:115144.

[8] Pérez-Lombard L, Ortiz J, Pout C. A review on buildings energy consumption information. Energy Build 2008;40:394–8.

[9] Dodoo A, Gustavsson L, Sathre R. Primary energy implications of ventilation heat recovery in residential buildings. Energy Build 2011;43:1566–72.

[10] Li B, Wild P, Rowe A. Performance of a heat recovery ventilator coupled with an air-to-air heat pump for residential suites in Canadian cities. J Build Eng 2019;21:343–54.

[11] Mardiana-Idayu A, Riffat SB. Review on heat recovery technologies for building applications. Renew Sustain Energy Rev 2012;16:1241–55.

[12] Zheng LJ, Kang HW. A passive evaporative cooling heat sink method for enhancing low-grade waste heat recovery capacity of thermoelectric generators. Energy Convers Manage 2022;251:114931.

[13] A. Chen, H. Liu, C. Ran, C. Wang. Economic analysis on application of exhaust air heat recovery in existing public buildings in the severe cold regions, 2015.

[14] Kuusk K, Kalamees T, Maivel M. Cost effectiveness of energy performance improvements in Estonian brick apartment buildings. Energy Build 2014;77:313–22.

[15] Becchio C, Corgnati SP, Vio M, Crespi G, Prendin L, Ranieri M, et al. Toward NZEB by optimizing HVAC system configuration in different climates. Energy Procedia 2017;140:115–26.

[16] Ploskić A, Wang Q. Evaluating the potential of reducing peak heating load of a multi-family house using novel heat recovery system. Appl Therm Eng 2018;130:1182–90.

[17] Wang Y, Zhao F-Y, Kuckelkorn J, Spliethoff H, Rank E. School building energy performance and classroom air environment implemented with the heat recovery heat pump and displacement ventilation system. Appl Energy 2014;114:58–68.

[18] Fehrm M, Reiners W, Ungemach M. Exhaust air heat recovery in buildings. Int J Refrig 2002;25:439–49.

[19] Wang M, Deng C, Wang Y, Feng X. Exergoeconomic performance comparison, selection and integration of industrial heat pumps for low grade waste heat recovery. Energy Convers Manage 2020;207:112532.

[20] Diaz de Garayo S, Martínez A, Astrain D. Optimal combination of an air-to-air thermoelectric heat pump with a heat recovery system to HVAC a passive house dwelling. Appl Energy 2022;309:118443.

[21] Tan Z, Feng X, Wang Y. Performance comparison of different heat pumps in low-temperature waste heat recovery. Renew Sustain Energy Rev 2021;152:111634.

[22] Wang L, Ma G, Ma A, Zhou F, Li F. Experimental study on the characteristics of triplex loop heat pump for exhaust air heat recovery in winter. Energy Convers Manage 2018;176:384–92.

[23] Bertsch SS, Groll EA. Two-stage air-source heat pump for residential heating and cooling applications in northern U.S. climates. Int J Refrig 2008;31:1282–92.

[24] Saini P, Paolo B, Fiedler F, Widén J, Zhang X. Techno-economic analysis of an exhaust air heat pump system assisted by unglazed transpired solar collectors in a Swedish residential cluster. Sol Energy 2021;224:966–83.

[25] Jia X, Ma G, Zhou F, Liu S, Wu G, Sui Q. Experimental study and operation optimization of a parallel-loop heat pump for exhaust air recovery in residential buildings. J Build Eng 2022;45:103468.

[26] Feist W, Schnieders J, Dorer V, Haas A. Re-inventing air heating: Convenient and comfortable within the frame of the Passive House concept. Energy Build 2005;37:1186–203.

[27] Fracastoro GV, Serraino M. Energy analyses of buildings equipped with exhaust air heat pumps (EAHP). Energy Build 2010;42:1283–9.

[28] Long J, Xia K, Zhong H, Lu HYA. Study on energy-saving operation of a combined heating system of solar hot water and air source heat pump. Energy Convers Manage 2021;229:113624.

[29] Qiu G, Wei X, Xu Z, Cai W. A novel integrated heating system of solar energy and air source heat pumps and its optimal working condition range in cold regions. Energy Convers Manage 2018;174:922–31.

[30] Li J, Fan Y, Zhao X, Bai X, Zhou J, Badiei A, et al. Design and analysis of a novel dual source vapor injection heat pump using exhaust and ambient air. Energy Built Environ 2022;3:95–104.

[31] Fan Y, Zhao X, Li J, Li G, Myers S, Cheng Y, et al. Economic and environmental analysis of a novel rural house heating and cooling system using a solar-assisted vapour injection heat pump. Appl Energy 2020;275:115323.

[32] Chen J, Zhang Z, Zhang G, Wang D. Energy, exergy, economic and environmental analysis of a novel direct-expansion solar-assisted flash tank vapor injection heat pump for water heater. Energy Convers Manage 2022;254:115239.

[33] Tello-Oquendo FM, Navarro-Peris E, Gonzálvez-Maciá J. Comparison of the performance of a vapor-injection scroll compressor and a two-stage scroll compressor working with high pressure ratios. Appl Therm Eng 2019;160:114023.

[34] Yang S, Tian J, Jiang H. Corresponding state principle based correlation for the thermal conductivity of saturated refrigerants liquids from Ttr to 0.90Tc. Fluid Phase Equilib 2020;509:112459.

[35] Farrance I, Frenkel R. Uncertainty of Measurement: A Review of the Rules for Calculating Uncertainty Components through Functional Relationships. Clin Biochem Rev 2012;33:49–75.

[36] Higham EH. In: Mechanical Measurements. Elsevier; 1985. p. 108–16. https://doi.org/10.1016/B978-0-408-01231-7.50014-3.

[37] Design Code for heating ventilation and air conditioning of civil buildings (GB 50736-2012). MOHURD, China, 2012.